Hydro-Sedimentary Processes of a Plunging Hyperpycnal River Plume Revealed by Synchronized Remote Imagery and Gridded Current Measurements

Stan Thorez[1] [ORCID], **Ulrich Lemmin[2]** [ORCID], **D. Andrew Barry[2]** [ORCID], and **Koen Blanckaert[1]** [ORCID]

[1]Research Unit of Hydraulic Engineering and Environmental Hydromechanics (HYDEN), Institute of Hydraulic Engineering and Water Resources Management (WIH), Faculty of Civil and Environmental Engineering, Technische Universität Wien (TUW), Vienna, Austria, [2]Ecological Engineering Laboratory (ECOL), Institute of Environmental Engineering (IIE), Faculty of Architecture, Civil and Environmental Engineering (ENAC), Ecole Polytechnique Fédérale de Lausanne (EPFL), Lausanne, Switzerland

Abstract The present knowledge of plunging hyperpycnal river plumes is mainly based on two-dimensional (confined) laboratory experiments. Several hypotheses on three-dimensional (unconfined) flow processes have been made, but not tested in situ. In this field study, the dominant three-dimensional hydro-sedimentary processes related to unconfined plunging were elucidated by synchronizing autonomous time-lapse camera images with boat-towed acoustic Doppler current profiler measurements. It was found that the flow field complies with two-dimensional conceptualizations along the plume centerline. Perpendicular to the centerline, the plume slumped laterally due to its density excess and simultaneously converged laterally due to its vertical divergence. This combination led to a narrowing of the plume near the surface, resulting in a sediment-rich triangle-shaped pattern on the surface near the inflow, and a rather stable width near the bed. The formation of secondary flow cells transporting riverine water and suspended particulate matter (SPM) away from the plume near the bed, up toward the surface and back toward the plume near the surface, was revealed. An increase of the average SPM concentration and the SPM flux in the main flow direction indicates net sediment erosion under the investigated conditions of high discharge and sediment load. This suggests transient storage of sediment during conditions of lower discharge and sediment load, and high morphological activity in the plunging area. These findings allowed extending a classical conceptual plunging model to laterally unconfined sediment-laden plunging inflows for conditions of well-mixed ambient water in the plunging region and inflow densimetric Froude numbers exceeding 1, common in nature.

Plain Language Summary When higher density river water flows into a lower density lake or reservoir, the river water forms a plume that dives down (referred to as plunging) toward the bottom of the lake or reservoir and flows along its bottom as an underwater current. Previously, the processes related to plunging were poorly understood in typical lake settings. In this study, these processes were investigated by combining camera images of the lake surface and measurements along a grid of both the currents and sediment concentration of the Rhône River plume entering Lake Geneva (Switzerland). Previously predicted processes occurring in the river plume, including plunging along its axis and a combination of lateral collapsing and contracting motions, were confirmed to exist. Other processes, including two swirling flows transporting river water and sediment back toward the surface, were revealed. These contribute to the spreading and mixing of river water and sediment in different ways from those measured in laboratory representations of reservoirs. Furthermore, the plunging river water eroded the lake bed near the river mouth during the measurements. The results from this study lead to a better understanding of plunging flows in lakes and allow for improved modeling and better predictions of such flows.

1. Introduction

Riverine inflows are an important input of oxygen, sediment, pollutants, nutrients, momentum and heat for lakes, reservoirs and oceans. They affect water quality and reservoir storage capacity and can exacerbate hazards (Allan et al., 1983; Fink et al., 2016; Lambert et al., 1984; Loizeau & Dominik, 2000; Schleiss et al., 2016; Vincent et al., 1991; Wüest et al., 1988; Wurtsbaugh et al., 2019). When riverine inflows are hyperpycnal (negatively buoyant) with respect to the receiving water body, they plunge and form a gravity-driven density current near the

bed (Fischer et al., 1979; Forel, 1885; Singh & Shah, 1971, Figure 1). Such a current, also called an underflow (or turbidity current when the density excess is caused by a high sediment concentration), will continue downslope until a layer of neutral buoyancy is reached, after which it will detach from the bed and form an interflow (Piton et al., 2022; Soulignac et al., 2021). If no such layer is encountered (due to the absence of stratification of the receiving water body or more generally a large enough density excess of the underflow), the underflow may continue into the deepest layers of the hypolimnion where it may form canyons (Forel, 1885, 1892; Girardclos et al., 2012). In this paper, the continuous current consisting of inflow, plunge, underflow and interflow will be referred to as the "river(ine) plume" or "plume" (Figure 1). Mixing processes which involve the entrainment of ambient water into the riverine plume and/or detrainment of riverine water away from it, change the density of the plume and therefore its density excess (buoyancy), as well as its thickness and discharge (Akiyama & Stefan, 1984). Of particular interest are mixing processes associated with plunging, since they pre-condition the upstream boundary conditions for the subsequent underflow and thereby influence the pathway and eventual fate of all riverine input constituents (Rueda et al., 2007).

Despite the importance of the plunging process, little is known about the hydrodynamic and sedimentary processes in the plunging area, particularly in the field. Thus far, most studies on plunging inflows were performed in laboratory settings in laterally confined (see Figure 2 for definition sketch), mildly sloped configurations, and without sediment. Some of these studies were performed in constant-width laboratory channels (Arita & Nakai, 2008; Fleenor, 2001; Lamb et al., 2010; Lee & Yu, 1997; Singh & Shah, 1971), and others in diverging configurations (Akiyama & Stefan, 1987; Hauenstein, 1983; Johnson, Ellis, et al., 1987; Johnson et al., 1989; Johnson, Farrell, et al., 1987; Stefan & Johnson, 1989). Both are representative of river-dammed reservoirs (Figures 1 and 2). Most of these studies focused on flow visualization, with a few of them including single velocity profiles; none, however, carried out velocity transects. These studies led to the development of the conceptualization shown in Figure 1 (adapted from Fischer et al., 1979; Singh & Shah, 1971), where plunging occurs at the plunging line across the entire river width. The plunging line is located at a constant distance x_p from the river mouth, making flow processes essentially two dimensional. This plunging, in turn, drives a return flow in the ambient water toward the plunging line, leading to surface flow convergence at the plunging line. Furthermore, these studies hypothesized that the inflow densimetric Froude number $\mathrm{Fr_d}$ is the dominant control parameter for the plunging process. It is defined as:

$$\mathrm{Fr_d} = \frac{U_0}{\sqrt{g'H}}, \tag{1}$$

where U_0 is the average velocity of the inflowing river water, $g' = g\Delta\rho/\rho_a$ is the reduced gravity defined as the magnitude of gravitational acceleration g times the density difference between the river and the receiving ambient lake surface water $\Delta\rho$, normalized by the lake surface water density ρ_a, and H is the river depth at the mouth.

Field investigations of plunging flows are scarce. Elder and Wunderlich (1972), Hebbert et al. (1979), Fischer and Smith (1983), and Fleenor (2001) used passive tracers, such as injected Rhodamine WT, temperature and salinity of the plume and the ambient water, to quantify the amount of mixing in laterally confined plunging inflows into Chilhowee Reservoir and Norris Reservoir in Tennessee, USA, Lake Mead in Nevada, USA, Whiskeytown Reservoir in California, USA, and Wellington Reservoir in Australia, respectively. They also included longitudinal-vertical (along the inflow axis) transect profiles of these passive tracers that indicate the location of the plunge, but do not reveal any details of the underlying flow processes. Vidal et al. (2012) presented longitudinal-vertical transects of passive tracers of a plunging river plume in Sau Reservoir in Spain along with five vertical velocity profiles, which made evident the flow transition from open-channel flow through plunging into an underflow. They also showed that the presence of an interflow led to an increase of Chlorophyll *a* concentration, further emphasizing the influence of plunging inflows on local water quality. Kostaschuk et al. (2018) measured a longitudinal-vertical transect of the velocity of a laterally confined plunging inflow into Xiaolangdi Reservoir in China. The profile shows the location of the plunge and intermittency in the velocity profile of the subsequent underflow, which they referred to as "pulsing" after Best et al. (2005).

Plunging in laterally unconfined, steep-sloped configurations (see Figure 2 for definition sketch) has received even less attention. In such configurations, the plunging inflowing river water is free to move in the lateral direction (perpendicular to the river plume centerline). An abrupt change in bed slope at the river mouth prevents vertical confinement. These conditions are mainly representative of lakes, although they also have been found
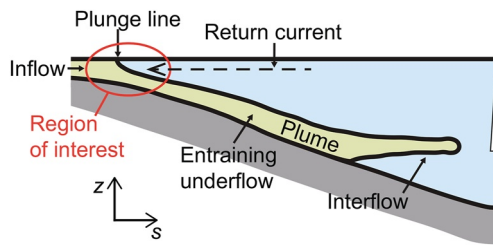
Figure 1. Conceptualization of a plunging inflow into a stratified ambient water body as adapted from Singh and Shah (1971) and Fischer et al. (1979). The red ellipse indicates the plunging area, which is the region of interest for the present study. The terms "river(ine) plume" or "plume" (marked in green) refer to the continuous current consisting of inflow, plunge, underflow and interflow. Note that an interflow does not form when the ambient water body is unstratified or when the excess density of the plume is strong enough for it to reach the bottom of the ambient water body.

to occur in man-made reservoirs (Cortés et al., 2014) and oceans (Katz et al., 2015; Mulder et al., 2003). Spigel et al. (2005) measured the temperature of a laterally unconfined inflow into Lake Taupo, New Zealand, along longitudinal-vertical and lateral-vertical transects. The measured patterns comply with the classic conceptualization of Fischer et al. (1979) in the longitudinal direction and indicate that the plunged water forms a wide and well-defined underflow plume in the lateral direction. One velocity profile taken downstream of the plunge shows that a return flow toward the plunge can also form in laterally unconfined configurations. Cortés et al. (2014) measured two lateral-vertical transects of the longitudinal velocity of a laterally unconfined plunging flow into Béznar Reservoir, Spain, but these were situated behind the plunge and did not provide any details of the flow dynamics. Spigel et al. (2005) and Cortés et al. (2014) also quantified the amount of plunging mixing taking place in their respective systems using temperature measurements, and a combination of mean plume velocities and temperature measurements, respectively. They found values of mixing up to an order of magnitude larger than those found in laterally confined configurations, indicating that certain flow processes that increase the intensity of plunging mixing might exist in laterally unconfined configurations, but do not exist in laterally confined configurations.

Mulder et al. (2003) included aerial photographs of the laterally unconfined plunging inflows of the Rusizi River into Lake Tanganyika, Tanzania (Figure 3a) and of a Jökulhlaup into the Atlantic Ocean seaward of Skeidarar-sandur, Iceland. In both photographs, the plumes of sediment-rich water exhibit a triangle-shaped pattern at the surface near the inflow, with its base at the river mouth and leading toward a narrow tip in the positive (away-from-mouth) longitudinal direction. They also exhibit irregularly shaped wakes stretching from the tip of the triangle-shaped surface patterns (Figure 3a) in the same direction. Mulder et al. (2003) referred to these wakes as the "plunging area," hypothesizing that the plunging itself happened in these wakes.
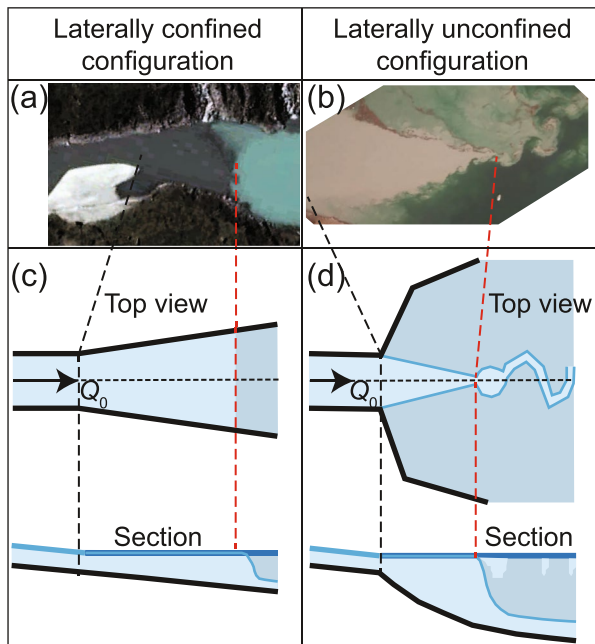
A total of 25 examples of laterally unconfined inflows in lakes and reservoirs that produce similar triangle-shaped patterns of sediment-rich water at the surface of the receiving water body were found on Google Earth and listed in Table A1. A limited selection of these inflows is presented in Figure 4. Figures 4d and 4h show two images of the Rusizi River delta in Lake Tanganyika (the same inflow shown by Mulder et al., 2003). The images demonstrate that in deltaic river inflows, each separate river branch can form a plume with a triangle-shaped surface pattern, which can coalesce with its neighboring plumes under high flow conditions to form a single surface pattern with a scalloped edge. Soulignac et al. (2021) analyzed several 20-image sequences of the Rhône River inflow into Lake Geneva, Switzerland, each taken over 27 hr. The sequences show that even under highly dynamic conditions, the triangle-shaped surface pattern is a persistent feature.

Figure 2. Examples of (a) a laterally confined inflow (Dranse de Bagnes Torrent into Lake Mauvoisin; image retrieved from Google Earth on 22 February 2023, additional image credits © 2023 Maxar Technologies, image modified by increasing contrast) and (b) a laterally unconfined inflow (Rhône River into Lake Geneva; image by the authors), with conceptual sketches of both configurations in panels (c, d). In panels (c, d), black dashed lines: end of river channel; red dashed lines: location of plunging line in panel (c) and furthest offshore plunging location in panel (d).

Best et al. (2005) measured one longitudinal-vertical velocity transect and provided an aerial photograph of the laterally unconfined inflow of Lillooet River into Lillooet Lake, British Columbia, Canada. The aerial photograph (Figure 3c) shows a distinct scalloped plunging line, which can likely be explained by the coalescence of triangle-shaped surface patterns similar to the case of the Rusizi River at Lake Tanganyika (Figures 4d and 4h). Best et al. (2005) mention that this plunging line was characterized by shifting lobes that advanced ~200 m into the lake before switching laterally. The velocity transect shows a return flow at the surface and traces of an underflow and an interflow. This velocity transect was repurposed by Kostaschuk et al. (2018). Their version of the transect is shown in Figure 3d and indicates clearly the location of the plunge.
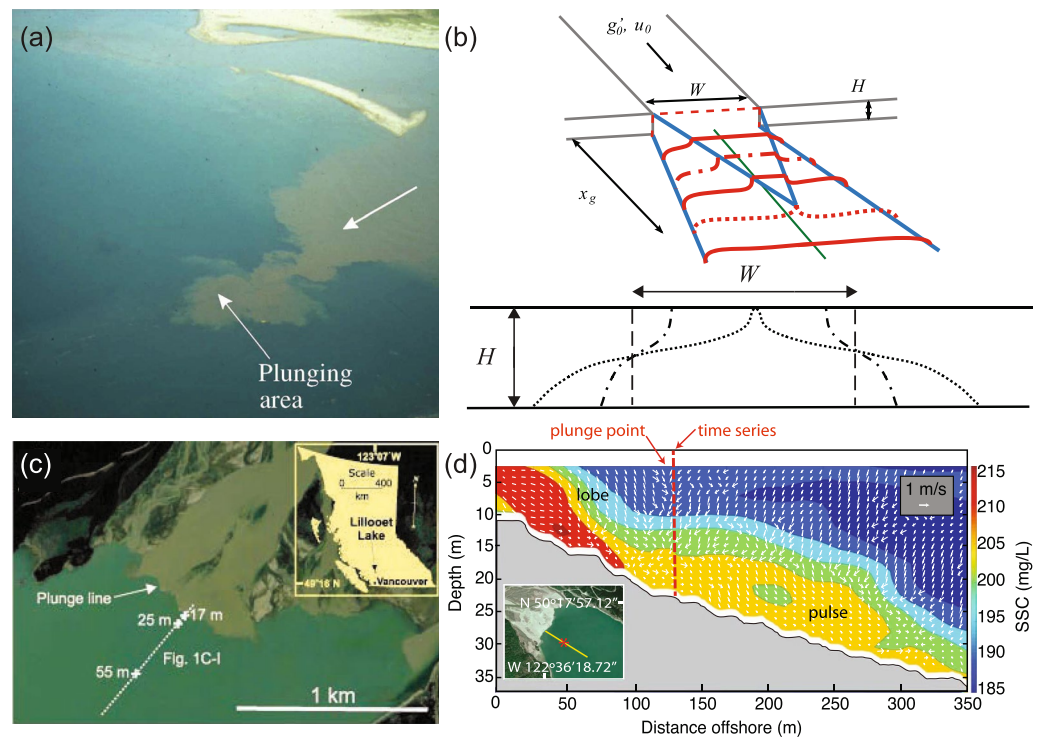
Figure 3. Figures taken from the literature illustrate the existing hypotheses of the laterally unconfined plunging process. (a) Aerial photograph of the laterally unconfined plunging inflows of the Rusizi River into Lake Tanganyika, Tanzania from Mulder et al. (2003; photo by Tiercelin et al., 1987, 1992), indicating the plunging area as hypothesized by them. (b) Conceptual sketches of a laterally unconfined hyperpycnal inflow by Hogg (2014), detailing their hypothesis that such an inflow undergoes lateral slumping caused by gravitational forcing and accompanied by baroclinic vorticity production, leading to the formation of a triangle-shaped surface pattern. W and H indicate the width and height of the inflow channel, respectively, while x_g indicates the maximum extent of the triangle-shaped surface pattern. The reduced gravity at the inflow is indicated by g_0' and the inflow velocity by u_0. (c) Aerial photograph of the laterally unconfined inflow of the Lillooet River into Lillooet Lake, British Columbia, Canada (Best et al., 2005) showing a scalloped plunging line and the location of their longitudinal-vertical transect shown in (d). (d) Longitudinal velocity (arrows) and suspended sediment concentration (SSC; colors) along the longitudinal-vertical transect (white dotted line) shown in (c) as repurposed by Kostaschuk et al. (2018), showing the location of the plunge.

Hogg et al. (2013) and Hogg (2014) theorized that for Fr_d numbers slightly larger than unity, buoyancy forces dominate lateral entrainment for laterally unconfined, hyperpycnal inflows entering a lake. They note that the gravitational forcing causes lateral slumping accompanied by baroclinic vorticity generation (see Figure 3b for a sketch of their conceptual flat-bed model). Hauenstein and Dracos (1984) alluded to this effect in a definition sketch of the flow structure of a laterally unconfined plunging flow, without describing it in detail. Hogg et al. (2013) and Hogg (2014) visually identified a plunging area at the inflow of the Canale Italsider into Lake Iseo. For this, they relied on a buildup of flotsam that indicated the presence of a convergence zone, which they called the plunging curve, at about 30–50 m from the river mouth.

Numerical work on laterally unconfined plunging inflows was performed by Tseng and Chou (2018) and Shi et al. (2022). The computational domain of Tseng and Chou (2018) consisted of an idealized geometry simulating an arbitrary river inflow into an ocean, while that of Shi et al. (2022) consisted of an idealized geometry simulating the Rhône River inflow into Lake Geneva at a scale of 1:60. Both studies performed simulations of saline inflows, with Tseng and Chou (2018) also simulating sediment-laden inflows. Their model results showed the formation of a triangle-shaped surface pattern and the lateral slumping of the inflow plume under baroclinic forces, reinforcing the hypothesis of Hogg et al. (2013) and Hogg (2014). Shi et al. (2022) confirmed these processes in laboratory measurements. Additionally, their numerical experiments suggested the formation of a secondary flow cell on each side of the plume edge near the bed in the lateral-vertical transect and an increase in the mixing rate in the plunging region for laterally unconfined configurations compared to laterally confined configurations.
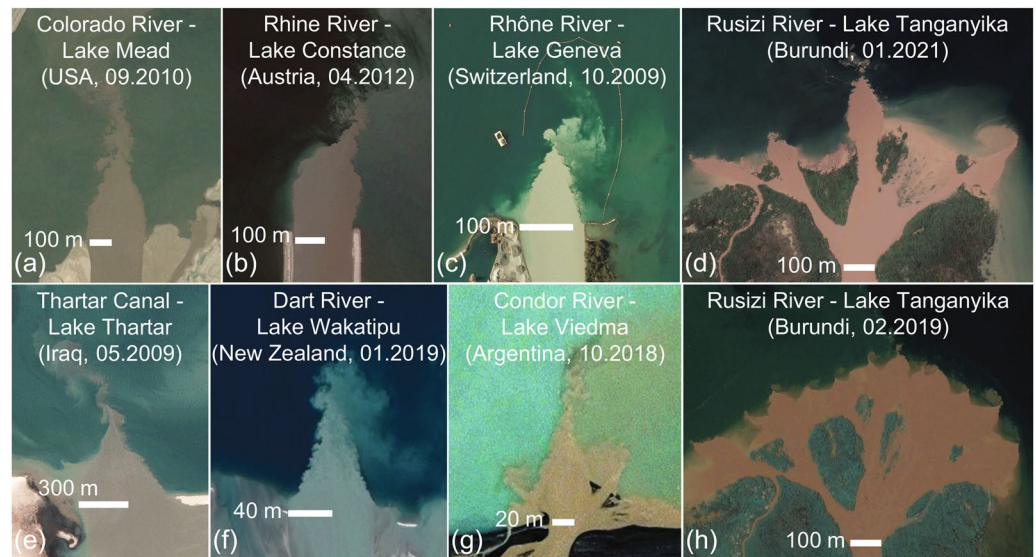
Figure 4. Selection of satellite images showing various inflows in lakes and reservoirs, each exhibiting at least one triangle-shaped pattern of sediment-rich water at the surface close to the inflow. Images (d, h) of the same river delta illustrate the potential of nearby plumes to coalesce under high flow conditions in panel (h). Images retrieved from Google Earth on 22 February 2023, additional image credits (a) USDA/FPAC/GEO, (d, e, f) © 2023 Maxar Technologies, (g, h) © 2023 CNES/Airbus. Image (g) modified by increasing contrast.

Mulder et al. (2003), Hogg et al. (2013), and Hogg (2014) presented their hypotheses on the dominant flow processes related to plunging. Little laboratory and numerical work (Shi et al., 2022; Tseng & Chou, 2018) exists to support and expand upon the hypothesis of Hogg et al. (2013) and Hogg (2014), and none of these studies include process-resolving field measurements. The sparsity of direct measurements of plunging flows could be attributed to the difficulty of measuring such systems. Reasons for this difficulty include the intrinsic instability of the system leading to intermittent flow patterns (Best et al., 2005; Kostaschuk et al., 2018) and the low flow velocities that are expected to occur, especially in the velocity components perpendicular to the main flow direction (Hogg, 2014; Hogg et al., 2013; Shi et al., 2022; Tseng & Chou, 2018).

Sedimentary processes related to plunging have, to the authors' knowledge, never been investigated in detail. Kostaschuk et al. (2018) provided suspended particulate matter (SPM) measurements of a plunging inflow along one longitudinal-vertical transect (Figure 3d), but the concentrations they measured were rather low ($O(SPM) = 0.2$ kg m^{-3}) and they did not provide any information on the sediment budget, whether erosion or deposition occurred, or the influence on the local bathymetry. Piton et al. (2022) measured SPM along multiple lateral-vertical transects in the interflow resulting from the inflow of the Rhône River into Lake Geneva. They also computed the flux of SPM, defined as

$$Q_{\text{SPM}} = \iint_S u_s(n, z) SPM(n, z) \, dS, \tag{2}$$

where S is the cross-sectional area of the plume, u is the local velocity, s is the main (longitudinal) flow direction, and n and z are the lateral and vertical directions perpendicular to the main flow direction, respectively. However, their results do not provide details of the sedimentary processes in the plunging region, since their nearest transect was 400 m from the mouth.

In this study, the hydro-sedimentary processes of a laterally unconfined plunging inflow into a lake are investigated in the field. The main research questions addressed are:

- Can the dominant three-dimensional hydro-sedimentary processes related to plunging be resolved for the first time using transect field measurements?
- What is the three-dimensional flow structure of a plunging plume and, in particular, where is the plunge located?
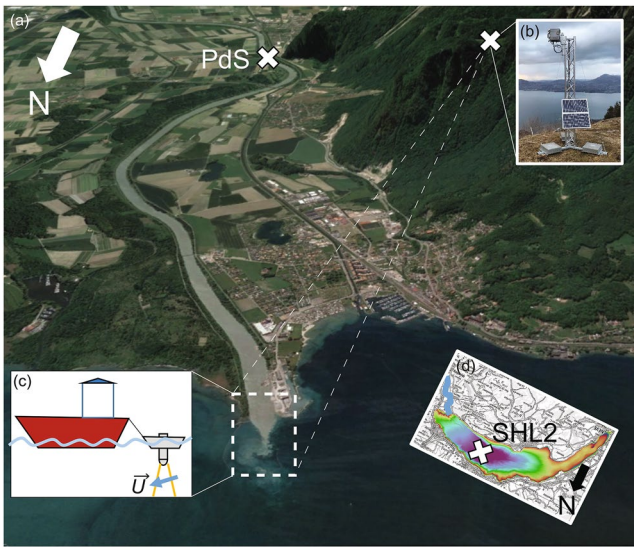
Figure 5. (a) Satellite image of the Rhône River inflow into Lake Geneva featuring a triangle-shaped surface pattern formed by the river plume (inside the white dashed-lined rectangle which delimits the study area) and the location of the Porte du Scex (PdS) hydrological measurement station on the Rhône River (white cross). The lake surface is monitored with (b) the remote time-lapse camera set-up (tagged to its location on a nearby mountain). (c) Currents are measured in the area with a boat-towed floating acoustic doppler current profiler (gray). (d) A bathymetrical map of Lake Geneva. The Rhône River is highlighted in blue (on the left) and the location of the CIPEL SHL2 hydrological measurement station is marked by a white cross. Image (a) retrieved from Google Earth on 22 February 2023, (d) retrieved from Swisstopo (https://www.swisstopo.admin.ch/) on 22 February 2023. Note that the lake map in panel (d) is shown rotated by 156° in order to match the Rhône River orientation with that in the satellite image.

- What are the sedimentary processes of a plunging plume and how do they influence the local bathymetry?
- How can existing conceptual models of plunging plumes be extended for unconfined configurations and flow-sediment-bed interactions?

2. Methods

2.1. Field Site and Conditions

Field measurements were performed near the Rhône River mouth in Lake Geneva, Switzerland on 26 June 2019 from 12:15 to 14:00 CET.

Lake Geneva is a deep, peri-alpine, oligomictic lake. The ambient conditions in Lake Geneva were measured on 26 June 2019 by the Commission Internationale pour la Protection des Eaux du Léman (CIPEL; Rimet et al., 2020) at their 309 m deep measurement station SHL2, located in the deepest part of the lake (Figure 5d). The average values for the lake near-surface water ($z = -15$ m to $z = 0$ m) temperature [°C] and salinity [g kg^{-1}] are given in Table 1. Lake water salinity was calculated directly from conductivity [µS cm^{-1}]. A density profile for the full depth of Lake Geneva was calculated from the temperature and the salinity after Chen and Millero (1986). It shows large density gradients in the 10 m nearest to the surface and a transition to a well-mixed regime in the deeper parts (Figure 6). The average density for the lake near-surface water is given in Table 1 and the maximum lake water density near the lake bottom is 1.0002×10^3 kg m^{-1}. The lake bed near the Rhône River mouth has an average slope of approximately 0.165 (corresponding to 7.4°) in the direction of the Rhône River axis.

The Rhône River originates in the Alps and has a nivo-glacial flow regime. Its mouth at Lake Geneva has a width of $W_0 = 126$ m and a depth of $H_0 = 4.4$ m, resulting in an aspect ratio of $H_0 W_0^{-1} = 0.035$. There is no delta development at the mouth due to regular bedload sediment dredging near the river mouth. At the FOEN-operated measurement station at Porte du Scex (Swiss Federal Office for the Environment, https://www.hydrodaten.admin.ch/de/2009.html), located about 6 km upstream of Lake Geneva (Figure 5), the river discharge [m^3 s^{-1}], temperature [°C], conductivity [µS cm^{-1}] and turbidity [Backscatter Unit (BU)] are measured continuously at 1-hr intervals, while the SPM [kg m^{-3}] is measured twice per week. In this study, a time series from 1 January 2019 until 30 September 2019 was used. River salinity [g kg^{-1}] was calculated directly from conductivity. For times when both turbidity and SPM values were available, a power law relationship between these parameters was fitted ($SPM = a \times turbidity^b$, where $a = 3.48 \times 10^{-4}$ kg m^{-3} BU^{-1} and $b = 1.20$ with $R^2 = 0.81$). This relationship is then used to estimate the SPM in the river using the turbidity values for each 1-hr interval. The river density was calculated from the temperature, the salinity and the SPM after Chen and Millero (1986). A one-dimensional hydraulic open-channel model based on the Bresse equation

Table 1

Average Values and Ranges During the Acoustic Doppler Current Profiler Measurement Campaign (26 June 2019 From 12:15 to 14:00) of the Most Relevant Parameters Relating to the Boundary Conditions

	Lake Geneva			Rhône river						Mouth	
Parameter	T_a [°C]	S_a [g kg^{-1}]	ρ_a [10^3 kg m^{-3}]	Q_r [m^3 s^{-1}]	T_r [°C]	S_r [g kg^{-1}]	SPM_r [kg m^{-3}]	ρ_r [10^3 kg m^{-3}]	Fr [ ]	$\Delta\rho\,\rho_a^{-1}$ [10^{-3}]	Fr_d [ ]
Value	14.58	0.19	0.9992	545.49	9.66	0.12	1.14	1.0006	0.15	1.37	4.04
Range				[521.33; 546.96]	[9.64; 9.71]	[0.12; 0.12]	[1.12; 1.18]	[1.0006; 1.0006]	[0.15; 0.15]	[1.36; 1.40]	[3.98; 4.08]

Note. Measured parameters: average lake surface water temperature T_a for Lake Geneva at CIPEL station SHL2; discharge Q_r and temperature T_r for the Rhône River at Porte du Scex. Calculated parameters: average lake surface water salinity S_a and density ρ_a for Lake Geneva; salinity S_R, suspended particulate matter SPM_r, density ρ_r and Froude number Fr for the Rhône River; relative density difference $\Delta\rho\,\rho_a^{-1}$ and densimetric Froude number Fr_d for the river mouth.
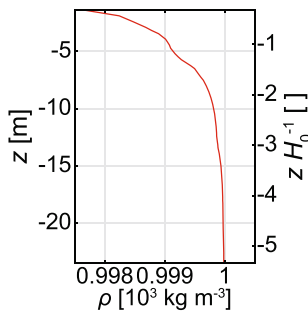
Figure 6. Density profile for the near-surface region of Lake Geneva calculated from the temperature and the conductivity measured at the CIPEL station SHL2 on the day of the acoustic doppler current profiler measurement campaign (26 June 2019). It shows strong gradients in the 10 m nearest to the surface and a transition to well-mixed water below.

(Bresse, 1860; Chow, 1959) was used to account for the time delay between the Porte du Scex station and the river mouth. The average values and ranges during the field measurement campaign of the most relevant river parameters are given in Table 1. Time series of the discharge and SPM for most of 2019 are presented in Figure 7.

The river and lake parameters mentioned above were used to calculate the relative density difference $\Delta\rho/\rho_a$, the Froude number $\mathrm{Fr} = U_0/\sqrt{gH}$, and the densimetric Froude number (Equation 1) at the inflow location. Their average values and ranges during the field measurement campaign are given in Table 1. Note that the contributions of both the SPM and the water temperature were the dominant factors with respect to the density excess.

2.2. Measurement Systems and Data Treatment

An autonomous RGB time-lapse camera system was set up at the Alpage de Chalavornaire (46°21′59″ N, 6°51′20″ E), a mountain viewpoint located 740 m above the lake surface level and 3 km south of the river mouth (Figure 5), to monitor the patterns formed by the sediment-rich river inflow at the lake surface. The camera (24 MP Nikon D3300 RGB camera with telephoto lens) took pictures at a frequency of one frame per minute and had a spatial resolution of about 0.3 m per pixel (Figure 8a). The images were geo-referenced and converted into a top view perspective (Figure 8b) using the method of Soulignac et al. (2021). In order to highlight steady flow and sedimentary features, a series of consecutive images were gray-scaled, averaged and the contrast was increased (Figure 8c), as will be detailed in the Results section.

Complementary to the surface patterns, the three-dimensional plume structure in the plunging area was obtained from boat-towed Acoustic Doppler Current Profiler (ADCP, see Figure 5c) measurements performed along a grid of longitudinal-vertical and lateral-vertical transects (see Figure 8b for transect locations). The location of these transects was guided by the synchronized time-lapse camera images that were monitored in quasi-real-time on the boat. One longitudinal-vertical transect (A-A), oriented approximately along the Rhône River axis, passed through the part of the river plume that was visible at the surface and extended beyond it. Three lateral-vertical transects (B-B, C-C and D-D) were oriented roughly perpendicular to the Rhône River discharge axis. Transects B-B and C-C were located well within the part of the river plume that was visible at the surface and transect D-D crossed

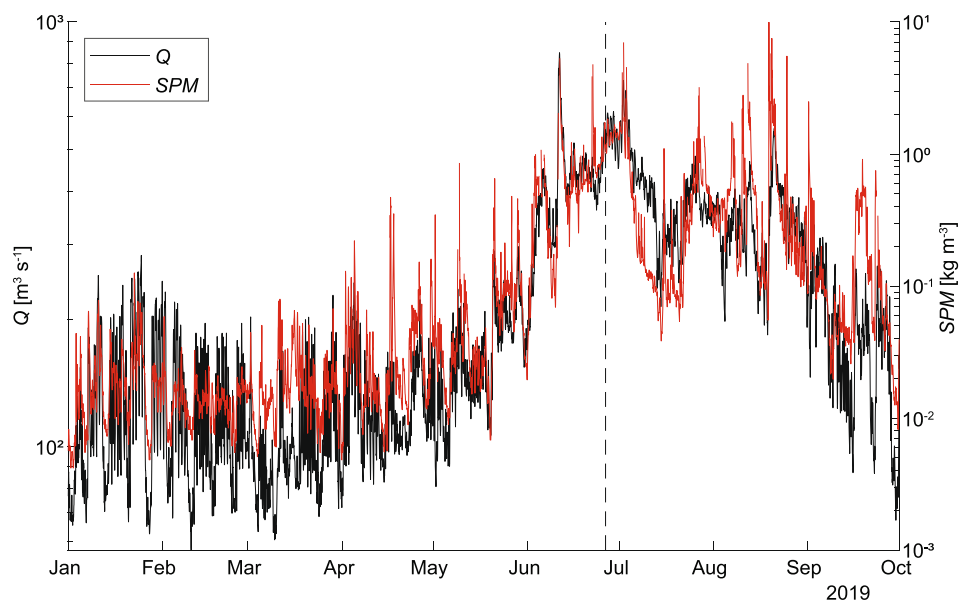**Figure 7.** Timeseries of the Rhône River discharge (Q; black) and suspended particulate matter (SPM; red) for most of the year 2019. The vertical dashed line indicates the date of the acoustic doppler current profiler field measurement campaign.
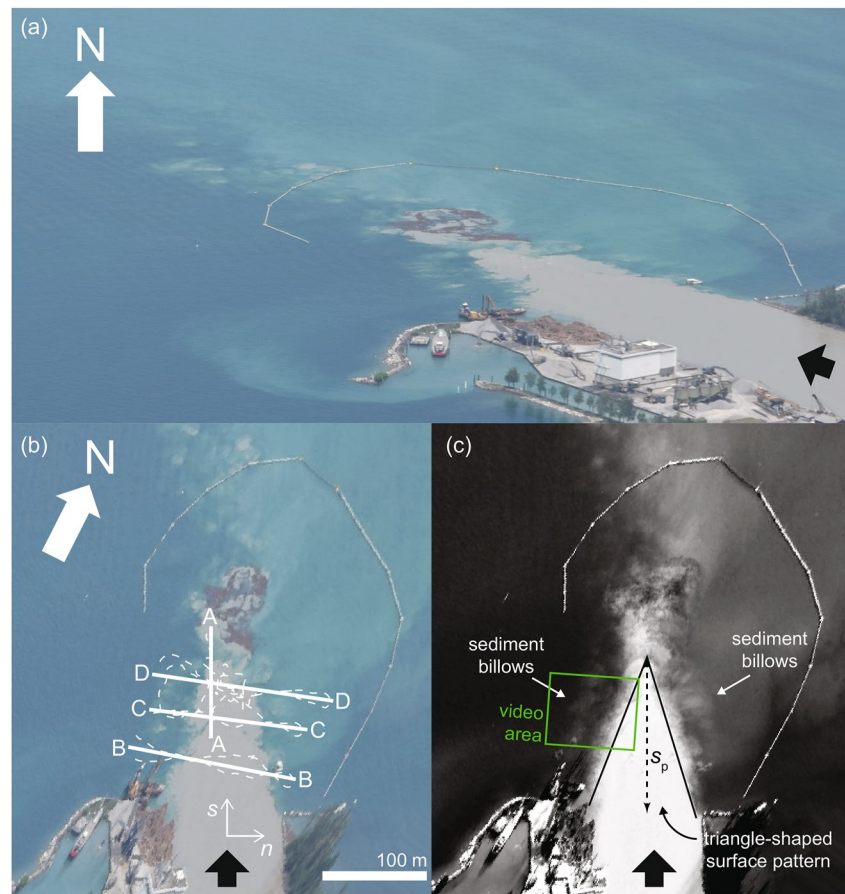
Figure 8. (a) RGB image taken during the acoustic doppler current profiler (ADCP) measurements by the remote time-lapse camera (see Figure 5 for camera location) showing the Rhône River inflow with its distinct gray-brown color due to a high sediment load. The dark brown-colored patch at the tip (furthest away from the mouth) of the triangle-shaped surface pattern is an accumulation of driftwood. The gray circular line surrounding the plume is a floating barrier intended to contain such driftwood. (b) RGB image shown in panel (a) geo-referenced and top-view-converted. The white overlay shows the boat trajectory of the ADCP measurements (dashed lines) and the resulting averaged-velocity transect locations (solid lines) for the longitudinal-vertical (A-A) and lateral-vertical (B-B, C-C and D-D) transects. (c) Average of eight consecutive images taken during the measurements of transect B-B, gray-scaled and contrast-enhanced. This image shows the triangle-shaped, sediment-rich surface pattern and billows of sediment-rich water at some lateral distance from the triangle-shaped surface pattern. The distance s_p indicates the maximum downstream extent of the triangle-shaped surface pattern. The approximate area captured in an aerial video taken on 2 July 2019 under similar environmental conditions is indicated by a green rectangle (Movie S1).

through the furthest longitudinal extent of the visible part of the river plume. For each lateral-vertical transect, 2 (B-B, C-C) or 3 (D-D) repetitions were performed in order to improve the resolution of the flow patterns in the presence of intermittent flow structures and flow velocities that were low compared to the boat velocity.

The downward-looking four-beam ADCP (300 kHz Teledyne RDI Workhorse Sentinel) was mounted on a catamaran with its transducers at 0.3 m below the surface and towed along the transect grid at approximately 0.7 m s^{-1}. Its bin size was set to 1 m, its blanking distance to 1 m and its sampling interval to 1–1.25 s. Location tracking was performed using a StarFish GPS Receiver at a sampling interval of 1 s. In order to improve flow velocity estimates from moving-boat ADCP measurements, the data treatment procedure of Vermeulen et al. (2014) was used (see Vermeulen, 2015, for the software package). In this procedure, the data of the multiple repetitions of one transect are projected onto the vertical plane that is defined by the smallest average distance to the measurement points and averaged in a raster of 5 m wide bins with variable height (O(1 m)). The velocity vector (u_s, u_n, u_z) was analyzed in an orthogonal coordinate system, where s corresponds to the longitudinal flow direction of the plume, n the lateral direction and z the vertical direction. The flow direction of the plume was defined by the average plume velocity, where the plume extent was defined by all bins with velocity larger than 0.1 m s^{-1} and excluding

any loose patches smaller than 10 bins. For longitudinal-vertical transect A-A, the plume extent was defined per bin column, and for lateral-vertical transects B-B, C-C and D-D, it was defined for the whole plume cross-section.

In addition to the velocity measurements, the ADCP backscatter intensity (measured simultaneously with the velocity) was converted to provide an estimate of the SPM using the Hydrac software package (Fromant, 2019; Fromant et al., 2020). In Hydrac, the average size of the sediment particles in suspension is required as an input parameter for the backscatter-SPM conversion. No sediment samples were taken during the present measurement campaign and information on sediment size distribution in the Rhône River-Lake Geneva confluence system is scarce. Burrus et al. (1989), Corella et al. (2014), Soulignac et al. (2021), and Piton et al. (2022) provide some values, but none of them apply to the plunging region. Therefore, the Porte du Scex turbidity-based SPM estimates were used to calibrate the average sediment size assumption. This was done by iteratively varying the average sediment size that was fed into Hydrac until the mean SPM over the plume core, $<SPM>$, in the lateral-vertical transect nearest to the river mouth (B-B, see Figure 8b) closely matched the turbidity-based SPM value estimated at Porte du Scex. It was assumed that no net erosion or deposition occurred in the last few km of the river before the mouth and the short distance ($\sim$60–70 m) between the mouth and the nearest lateral-vertical transect. The closest match between $<SPM>$ in transect B-B (1.20 kg m^{-3}) and the SPM estimated at Porte du Scex (1.15 kg m^{-3}) was obtained for an average sediment size of $d = 54$ μm. This average sediment size falls within the range of values reported in literature (Burrus et al., 1989; Corella et al., 2014; Piton et al., 2022; Soulignac et al., 2021), while the SPM values are an order of magnitude higher than those measured by Kostaschuk et al. (2018). The SPM estimates and the velocity field were then used in Equation 2, to calculate Q_{SPM} over the plume core in each of the lateral-vertical transects, and Q_{SPM} over a unit width of the plume core (notation: q_{SPM}) in each bin column along the longitudinal-vertical transect, in order to be able to predict whether deposition or erosion will occur during the plunging process under the existing boundary conditions. The ADCP backscatter intensity also provides the local bathymetry (Vermeulen et al., 2014).

3. Results

3.1. Time-Lapse Camera Imagery

Time-lapse camera images of the inflowing Rhône River plume (Figure 8) were taken simultaneously with the ADCP measurements along lateral-vertical transect C-C (see Figure 8b for transect locations). The averaged image (Figure 8c) shows that the river water plume forms a distinct and persistent triangle-shaped pattern at the surface, with the base at the river mouth and leading toward the tip in the positive s-direction. It extends out into the lake over a nondimensionalized distance of $s_p W_0^{-1} \approx 1.16$ (Figure 8). On the left and right side of this triangle-shaped surface pattern, at a nondimensionalized distance of $n W_0^{-1} \approx 0.24$ outside of the plume, a band of upwelling billows of sediment-rich water can be observed. It was observed visually in the field that these billows are generated intermittently at a minimum nondimensionalized distance of $s W_0^{-1} \approx 0.48$ from the river mouth and are transported away from the river mouth parallel to the plume, thereby creating the two bands of sediment-rich water in the averaged images (Figure 8c). Figures 8b and 8c show the presence of a patch of sediment-rich water littered with driftwood extending over a nondimensionalized distance of the order of $s W_0^{-1} \approx 0.80$ in the wake of the triangle-shaped surface pattern. In the field, it was visually observed that this larger patch consisted of smaller sub-patches and that the driftwood was mostly concentrated around the edges of these smaller sub-patches.

3.2. ADCP Current Transect Measurements

The velocity field was measured by the ADCP along the longitudinal-vertical (A-A) and the lateral-vertical transects (B-B, C-C and D-D) (Figure 9). The river water plume can be identified by a core of high positive u_s values in all transects. These velocities reach a maximum value of $u_s \approx 1.7$ m s^{-1} ($u_s U_0^{-1} \approx 1.7$, where U_0 was calculated from the river discharge at Porte du Scex and the river mouth dimensions as $U_0 = Q_r W_0^{-1} H_0^{-1} \approx 1$ m s^{-1}) in transect B-B. Phenomena observable in transect A-A include (numbers indicated in Figure 9): (i) a transition through plunging from open channel flow to underflow from $s W_0^{-1} \approx 0.85$ to $s W_0^{-1} \approx 1.00$, before the plume reaches a depth of $z = -15$ m ($z H_0^{-1} = -3.41$), with vertical velocities down to $u_z U_0^{-1} \approx -0.3$, and paired with the typical velocity profiles associated with those flows (e.g., Alavian, 1986; Sequeiros et al., 2010, for underflows), (ii) a return flow with velocities down to $u_s U_0^{-1} = -0.6$ toward the river mouth at the surface for $s W_0^{-1} > 0.90$ (confirmed in the field by the accumulation of driftwood at the plume
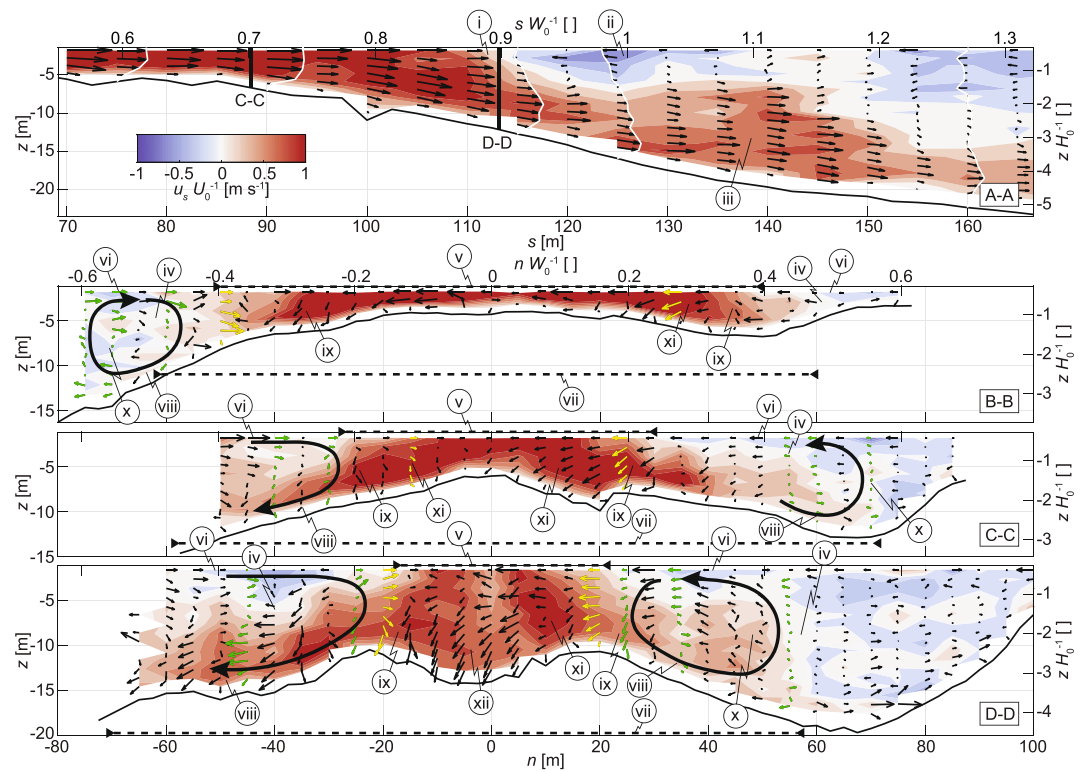
Figure 9. ADCP-based velocity patterns along the longitudinal-vertical (A-A) and lateral-vertical (B-B, C-C and D-D) transects, where positive (red) values indicate downstream velocities, while negative (blue) values indicate upstream velocities. The small black arrows indicate the in-transect velocities: longitudinal-vertical for A-A and lateral-vertical for B-B, C-C and D-D. The s coordinates indicate the longitudinal distance from the river mouth, the n coordinates indicate the lateral distance from the plume centerline and z coordinates indicate the depth below the water surface, while the sW_0^{-1}, nW_0^{-1}, and nH_0^{-1} coordinates indicate their normalized counterparts (with W_0 and H_0 the width and the depth of the river at the mouth, respectively). Note that transect A-A does not start at the river mouth; see Figure 8 for location. Five velocity profiles are highlighted by white lines. In transects B-B, C-C and D-D, lateral-vertical velocity profiles showing clearest the lateral convergence (yellow) and the secondary flow cells (green) are highlighted in color and the curved black arrows further accentuate the secondary flow cells. The black dotted lines with arrow heads indicate the plume width near the surface and the bed. The flow processes which are indicated in this figure by Roman numerals (i–xii), are described in detail in Section 3.2.

edge, not shown here) and (iii) a "bulge" in the underflow height profile and locally higher velocities between $sW_0^{-1} \approx 1.00$ and $sW_0^{-1} \approx 1.25$. Phenomena observed in transects B-B, C-C and D-D include: (iv) shear layers between the river plume and the ambient lake on both sides of the plume, (v) a narrowing of the plume in the upper half of the water column with increasing distance from the river mouth, accompanied by (vi) lateral velocities up to $u_n U_0^{-1} = \pm 0.6$ pointing toward the plume centerline close to the surface outside of the plume and partly overlaying it, (vii) an insignificant changing of the plume width in the lower half of the water column with increasing distance from the river mouth, accompanied by (viii) lateral velocities up to $u_n U_0^{-1} = \pm 0.5$ pointing away from the plume centerline close to the bed at the edge of the plume, (ix) locally higher downward velocities $u_z U_0^{-1} \approx -0.1$ at the inner edges of the plume, (x) upward velocities $u_z U_0^{-1} \approx 0.1$ at the outer edges of the plume, (xi) velocities pointing toward the plume centerline and downwards inside most of the plume, and (xii) highest downward velocities $u_z U_0^{-1} \approx -0.3$ at the center of the plume in transect D-D, which corresponds to the location of the transition from open channel flow to underflow in the longitudinal-vertical transect (Figure 9a). The combination of phenomena (v-viii) indicates the presence of a lateral slumping motion of the river plume. The combination of phenomena (vi, viii-x) indicates the presence of a secondary flow cell at each side of the plume, with velocities away from the plume near the bed and toward the plume near the water surface.
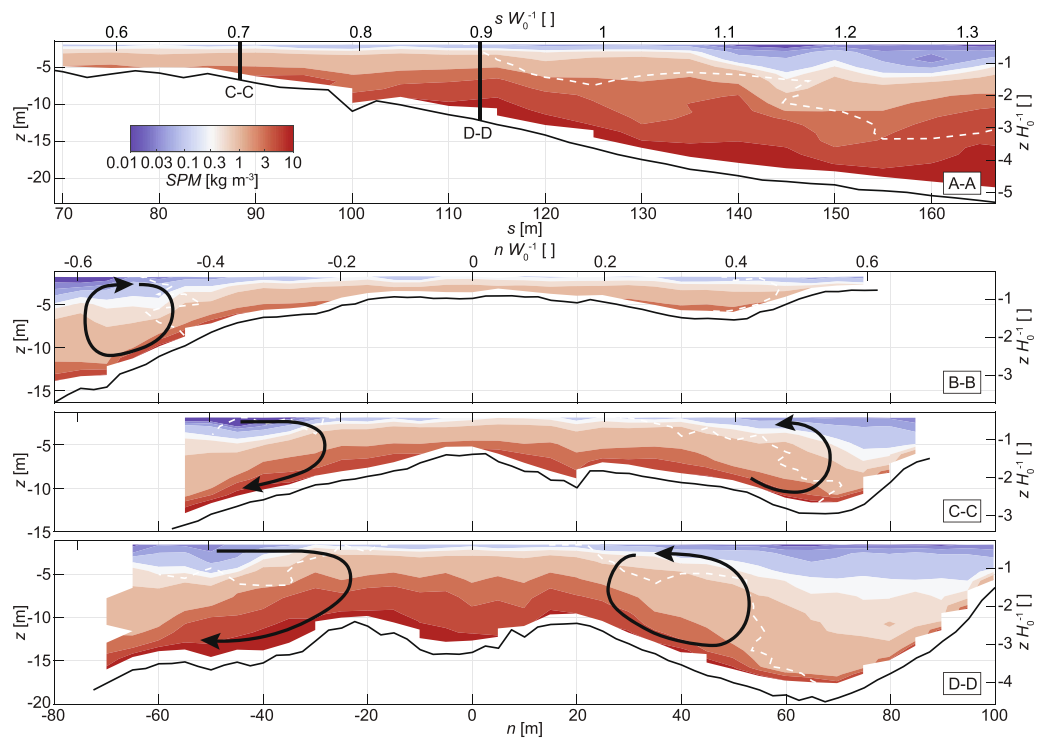
Figure 10. Acoustic doppler current profiler backscatter measurements converted to suspended particulate matter patterns along the longitudinal-vertical (A-A) and lateral-vertical (B-B, C-C and D-D) transects. The s coordinates indicate the longitudinal distance from the river mouth, the n coordinates indicate the lateral distance from the plume centerline and z coordinates indicate the depth below the water surface, while the sW_0^{-1}, nW_0^{-1}, and nH_0^{-1} coordinates indicate their normalized counterparts (with W_0 and H_0 the width and the depth of the river at the mouth, respectively). In transect A-A, the river mouth is located in the upper left direction. The black curved arrows indicate the location and direction of the secondary flow cells shown in Figure 9. The white dashed lines mark the 0.1 m s^{-1} longitudinal velocity contours.

3.3. ADCP SPM Transect Measurements

SPM patterns along all four transects (Figure 9) show that SPM values are higher near the bed and lower near the surface. In transect A-A, the SPM plume appears to thicken in the positive s-direction. The plunging location is not clearly visible, since high SPM values are found close to the surface beyond the plunging location. However, the "bulge" seen in the velocity profile (iii) also appears in the SPM. In transects B-B, C-C and D-D, the shape of the SPM plume roughly follows that of u_s. Subtle SPM billows coinciding with the location of upward velocities at the plume edges (ix) are visible as well. There is quantitative uncertainty in the conversion from ADCP backscatter to SPM, since the values of SPM are sensitive to the choice of the mean sediment diameter, which is provided as input parameter. However, a sensitivity analysis (not shown here), consisting of varying the mean sediment diameter in the range from 30 to 80 μm, shows that the shape of the SPM plume (Figure 10) is a robust result.

Generally, the SPM patterns reveal an increase in SPM in the positive s-direction. This trend is further substantiated by the $<SPM>$ and the q_{SPM} values along transect A-A, and the $<SPM>$ and the Q_{SPM} values over the plume extent in transects B-B, C-C and D-D (Figure 11). The $<SPM>$, the Q_{SPM} and the q_{SPM} values exhibit a strong increase within the plunging region in the positive s-direction. Downstream of the plunging region, they follow a more irregular pattern, coinciding with irregularities in transect A-A, such as the aforementioned "bulge" in both the velocity (Figure 9, iii) and the SPM (Figure 10) profiles. The robustness of the tendencies (particularly the increase within the plunging region) of Q_{SPM} and q_{SPM} in the positive s-direction (Figure 11) were confirmed as well by the sensitivity analysis mentioned in the previous paragraph.

The increase of the $<SPM>$, the Q_{SPM} and the q_{SPM} in the plunging region in the positive s-direction implies that during the measurement campaign, more sediment was eroded from the bed by the plunging flow and transported
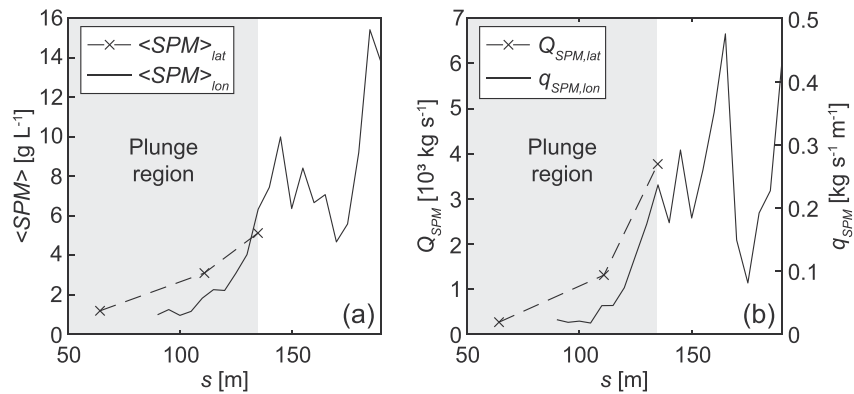
Figure 11. Evolution of (a) $<SPM>$ and (b) Q_{SPM} and q_{SPM} with distance from the river mouth.

in positive s-direction than was deposited. The theoretical capacity of the flow to erode the bed within the plunging region was investigated using the Shields number, which is defined as:

$$\theta = \frac{\rho u_*^2}{(\rho_s - \rho)gd},\tag{3}$$

where ρ is the density of the water, ρ_s the density of the sediment, and u_* the shear velocity. The latter was estimated from hydrodynamic theory by fitting the logarithmic velocity profile to the measured near-bed velocities (Graf, 1998). The Shields number, estimated from the field data, is larger than the critical Shields number necessary for the pickup and remobilization of sediment from the bed.

In transects B-B and C-C, the bathymetry exhibits a concave profile under the full width of the plume. Transect D-D however, features a convex bathymetry profile below the center of the plume.

4. Discussion and Conclusions

4.1. Relevance of the Results

The environmental conditions remained stable throughout the duration of the measurement campaign. Figure 7 shows that the measurement campaign coincided with some of the highest values of the discharge and SPM occurring during 2019. The inflow densimetric Froude number had a value between 4.5 and 6 for 27% of the Rhône River data set period, making its value during the measurement campaign (5.25, see Table 1) representative for a significant time of the year. Since many examples of plunging plumes with similar surface patterns can be found all over the world (see Figure 4; Table A1), the results described in this study can be expected to be relevant to these plumes. Therefore, this study provides valuable input data and validation data for laboratory and computational models of such plumes. Based on the results of the field measurements, the research questions defined in the Introduction section will now be addressed.

4.2. Innovative Measurement Set-Up Resolves Dominant Three-Dimensional Hydro-Sedimentary Plunging Processes

The results presented here provide the first in situ measurements of a hyperpycnal sediment-laden plunging river plume that resolve the three-dimensional flow and SPM patterns in detail. The combination of remote time-lapse imagery and ADCP velocity measurements proved to be mutually beneficial. The quasi-real-time remote time-lapse images allowed optimally locating the ADCP transects while performing the measurements (Figure 8b). Moreover, the remote time-lapse images of the plume surface patterns enriched the ADCP data interpretation and vice versa. For example, the clouds of sediment-rich water reappearing at the surface just outside the plume edges (Figure 8c) confirm the existence of secondary flow cells (Figure 9) and give an indication of their spatial extent. In addition, the three-dimensional ADCP velocity data reveal the underwater structure of the plunging plume (Figure 9) and explain the mechanisms underlying the triangular shape of the plume at the surface (Figure 8).

4.3. Three-Dimensional Flow Structure of a Plunging Plume and Plunging Location

The remote time-lapse images show that the plunging river plume forms a triangle-shaped pattern on the lake surface (Figure 8), which is in line with the observations of Mulder et al. (2003; Figure 3a), the conceptual model of Hogg et al. (2013) and Hogg (2014; Figure 3b) and the images that were gathered from Google Earth (Figure 4; Table A1). The maximum downstream extent of this pattern ($s_p W_0^{-1} \approx 1.16$) is slightly larger than that found by Shi et al. (2022) for an image of the same Rhône River-Lake Geneva inflow system, $s_p W_0^{-1} \approx 1.0$. This is due to the larger Fr_d at the inflow in the present study ($Fr_d \approx 4.0$ compared to $Fr_d \approx 3.2$ for Shi et al., 2022), a relationship they deduced from their numerical simulations. The same applies for Hogg et al. (2013), where $s_p W_0^{-1} \approx 0.6-1.0$ and $Fr_d \approx 2.6$. For Spigel et al. (2005), a larger $Fr_d \approx 8.3$ lead to a smaller $s_p W_0^{-1} \approx 0.8-1.0$. However, they mentioned that local bathymetrical features had a strong influence on the location of the plunge.

The ADCP measurements confirm that the classical conceptualization of the hydrodynamic processes of a plunging flow as shown in Figure 1 remains valid along the axis of the river inflow (Figure 9a). In the lateral direction (Figures 9b–9d), the measurements confirm that slumping caused by its density excess promotes the formation of the triangle-shaped surface pattern of the plume as hypothesized by Hogg et al. (2013) and Hogg (2014; Figure 3b), simulated numerically by Tseng and Chou (2018) and Shi et al. (2022), and measured in the laboratory by Shi et al. (2022). However, this is not the only process causing this surface pattern. Since no flow separation occurs at the bed, the increasing flow depth for increasing distance from the Rhône River mouth leads to vertical divergence of the flow, which is illustrated by the presence of downward velocities within the plume (vertical component of xi in Figure 9). Due to mass conservation, this is paired with a lateral convergence of the flow (Broekema et al., 2020), which is illustrated by the presence of velocities pointing toward the plume center-line within the plume (lateral component of xi in Figure 9). This lateral convergence also promotes the formation of a triangle-shaped surface pattern (Shi, 2023). The lateral slumping of the plume and lateral plume convergence result in different processes near the surface and near the bed. Near the surface, both have an average velocity component pointing toward the plume centerline, amplifying the narrowing of the plume near the surface and thus leading to a smaller maximum downstream extent of the triangle-shaped surface pattern. Near the bed, the lateral plume convergence with velocity components pointing toward the plume centerline compensates the effects of lateral slumping with velocity components pointing away from the plume centerline, thus stabilizing the plume width near the bed.

Analogous to the return flow toward the plunging line typically seen in laterally confined configurations, the ADCP measurements show the convergence of the near-surface velocities perpendicular to the edge of the triangle-shaped surface pattern. This was confirmed visually in the field by the buildup of driftwood at the surface of the river plume-lake water interface, similar to the observations that were made by Hogg et al. (2013) and Hogg (2014) at Lake Iseo. The return flow velocities reached comparatively high values, up to 60% (near ii and vi in Figure 9) of the average inflow velocity. A return flow was also measured in the field by Best et al. (2005, Lake Lillooet) and Kostaschuk et al. (2018, Lake Lillooet and Xiaolangdi Reservoir). Although they did not specify any velocity values, their velocity transect figures seem to indicate similarly strong return flow velocities with respect to the inflow velocities ($U_0 \approx 0.5 \text{ m s}^{-1}$, $u_{s,\text{backflow}} \approx -0.3 \text{ m s}^{-1}$). The return flow measured in Lake Taupo by Spigel et al. (2005) in a single vertical velocity profile was weak in comparison (∼5% of the inflow velocity), but that profile was located at $s W_0^{-1} \approx 10$, a distance where return flow velocities can be expected to be significantly lower. The laterally unconfined numerical models of Tseng and Chou (2018) and Shi et al. (2022) also produced a return flow. However, their velocity transects seem to indicate weaker return flow velocities compared to the inflow velocities (∼5% of the inflow velocity), even near the plume. The laterally unconfined laboratory experiments of Shi et al. (2022) produced a weak return flow (5%–10% of the inflow velocity) as well. Schuch et al. (2018, 2021) provide the velocity field of the return flow for numerical simulations of a laterally confined configuration, whose magnitude is also small (5%–10% of the inflow velocity). These low return flow magnitudes are tentatively attributed to the idealized numerical and laboratory boundary conditions. For laboratory experiments of laterally confined configurations, no quantifications of return flows could be found in the literature.

The ADCP velocity data reveal that the lateral slumping mechanism is accompanied by a secondary flow cell on each side of the plume stretching over the full local water depth, whose maximum upward velocity location moves toward the plume centerline in the positive *s*-direction (Figures 9c and 9d). The remote time-lapse images reveal that these secondary flow cells transport sediment-rich river water from near the bed to the water surface

at a distance of about a quarter of the plume width outside of the triangle-shaped surface pattern (Figure 8c). The "gap" of clear water between the triangle-shaped surface pattern and the sediment billows, indicates that these billows do not originate from the plume surface, but rather from upwelling in the water column. This is supported by Movie S1 (taken under similar environmental conditions on 2 July 2019 from above the edge of the triangle-shaped surface pattern; see Figure 8c for an approximation of the captured area) that shows upwellings of sediment-rich water, and by the presence of subtle billows at the plume edge in the SPM profiles that indicate upwellings (Figure 10). Furthermore, a conservative calculation according to Brown and Lawler (2003) shows that the typical settling velocity of 100 μm quartz sediment particles (which is almost twice the size (54 μm) determined in the Methods section) is approximately $v_{ss} = 6.5 \times 10^{-3}$ m s^{-1}, up to two orders of magnitude smaller than the upward velocities measured in the secondary flow cells. The presence of secondary flow cells exhibits strong similarities to the findings of Duguay et al. (2022). In their study on the confluence of the turbid, denser Coaticook River with the clear, less dense Massawippi River (Quebec, Canada), the density difference between these rivers was numerically found to drive longitudinally oriented vortices that, as observed in the field using aerial imagery, transport billows of sediment-rich water away from the turbid Coaticook River (and into the clear Massawippi River water) along the bed, upwards toward the surface and back toward the Coaticook River portion of the confluence. We hypothesize that these secondary flow cells are the dominant process with respect to the increased mixing in the plunging region in laterally unconfined field configurations (Cortés et al., 2014; Spigel et al., 2005) compared to laterally confined field configurations (Elder & Wunderlich, 1972; Fischer & Smith, 1983; Fleenor, 2001; Hebbert et al., 1979). Shi et al. (2022) also observed a secondary flow cell at each side of the plume in their numerical simulation of their unconfined laboratory configuration, yet they only extended across the lower half of the local water depth, rather than the full water depth. This might explain why Shi et al. (2022) found a plunging mixing rate that was lower than the ones measured in laterally unconfined configurations in the field by Spigel et al. (2005) and Cortés et al. (2014), although it was still higher than the values they found in their numerical simulation of a confined laboratory configuration. Possible reasons for the different flow cell sizes in the present study (Figure 9) and Shi et al. (2022) are the absence of sediment in their simulations, the constraints of boundary conditions, and their use of a simplified bathymetry.

The plunging of the inflowing river water happens within the depth layer where the lake is most stratified, a layer it breaks through due to its considerably larger density. Moreover, the density of the inflowing river water is larger than the maximum lake water density found near the lake bottom, which would imply that nominally, the density current formed after plunging would reach the deepest point of the lake. However, entrainment during plunging of the less dense near-surface lake water will decrease the density excess of the plume and increase the chance of an interflow at an intrusion depth well above the lake bottom. The influence of wind-driven background currents on the flow processes appears to have been negligible during the measurement campaign. Background currents near the Rhône River mouth are dominated by along-shore velocities caused by large-scale wind-driven gyres (Lemmin & D'Adamo, 1996). Advection by such along-shore currents would cause a deflection of the triangle-shaped surface pattern (Soulignac et al., 2021). Such deflection was not present during the measurement campaign as shown by the symmetrical water surface pattern (Figure 8c).

The high amount of SPM on the surface beyond the plunging location in transect A-A (Figure 10) matches the presence of a patch of sediment-rich water in the wake of the triangle-shaped surface pattern formed by the plume (Figures 8a–8c). These observations are similar to the image of the Rusizi River inflow into Lake Tanganyika included in Mulder et al. (2003), which also features a sediment-rich wake beyond the plunge (Figure 3a). Independent of which process induces the wake-patch, the presence of lateral slumping indicates that plunging takes place mainly along the edge of the triangle-shaped surface pattern of the plume and not mainly in its wake as hypothesized by Mulder et al. (2003; Figure 3a). The term "plunging point," which is often used in the two-dimensional description of plunging flows (Figure 1), is not appropriate here and rather a term suited better to this three-dimensional environment, such as "plunging line" (proposed by Hebbert et al., 1979) or "plunging curve" (proposed by Hogg et al., 2013), should be used in laterally unconfined configurations.

4.4. Sedimentary Processes and Their Effect on the Local Bathymetry

The investigation of the patterns and evolution of the SPM (Figures 10 and 11) demonstrates that under the conditions present during the measurement campaign (high river discharge and high river sediment load) the plunging process was predominantly erosive in nature. The similarity of flow and SPM patterns (Figures 9 and 10)

highlights that during the field measurements particulate matter was mainly picked up from the bed below the core of highest plume velocities and redistributed by the three-dimensional flow field. Assuming a long-term dynamic equilibrium between the flow and the bathymetry, these observations suggest that sediment is deposited in the plunging region under low river discharge and sediment load conditions, and that this sediment is remobilized under high river discharge and sediment load conditions which corresponds to our study. This transient storage and remobilization of sediment could play an important role, for example, in the triggering of turbidity currents further downstream (Lambert & Giovanoli, 1988; Parker et al., 1986). Furthermore, as literature suggests a strong influence of the local bathymetry on the location of the plunge (Fischer et al., 1979; Hebbert et al., 1979; Spigel et al., 2005), the authors expect that over time a changing plunging region bathymetry during alternating erosion- and deposition-dominated periods could lead to a change in the location of the plunge for the same inflow densimetric Froude number.

The irregular nature of the $<SPM>$ and the q_{SPM} values beyond the plunging region (Figure 11), coinciding with the irregular flow patterns (process (iii) in Figure 9) beyond this point, reinforce the hypothesis of Best et al. (2005) and Kostaschuk et al. (2018) that such irregular flow patterns might lead to spatial variations in bed erosion and deposition that could produce complex stratigraphic deposits such as those reported by Duringer et al. (1991).

The fact that the upwelling of sediment billows shows rather subtle traces in the SPM patterns (Figure 10) indicates that mostly finer sediment is being upwelled by the secondary flow cells. A relatively small concentration of such finer sediment can still lead to significant changes in turbidity as detected by the time-lapse camera (Figure 8c).

The local profile of the bathymetry (Figure 9), in particular the smaller local depth underneath the center of the surface plume and the larger local depth underneath the edges of the surface plume in transects B-B and C-C, may be the result of a flow process described by Shi et al. (2022). In their numerical simulations, they observed a detachment of the flow from the bed within the plunging region that resulted in lower longitudinal velocities near the bed along the plume centerline. Since their numerical domain had a fixed bed, this did not influence the bathymetry. In the case of the Rhône River inflow into Lake Geneva, however, the SPM might fill in such a low velocity zone and lead to the observed bathymetrical profile. The resulting shape of the local bathymetry in turn can be expected to feed back into the three-dimensional flow patterns.

4.5. Conceptualization

The main findings of the present study support an extension of the classical conceptual plunging model that remains valid for sediment-laden river inflows in unconfined configurations and includes flow-sediment-bed interactions. The extended conceptual model (Figure 12) includes: (a) flow processes observed in laterally confined plunging flows that were also observed in laterally unconfined plunging flows, such as the velocity field along the plume centerline, (b) previously hypothesized and simulated flow processes for laterally unconfined plunging flows that were confirmed in the present study, such as the lateral convergence and slumping of the plume and the resulting triangle-shaped surface pattern, and (c) newly revealed flow processes, such as the formation of secondary flow cells covering the full water column, the related sediment transport toward the lake surface, and the influence of the plunging on the local bathymetry.

Note that the proposed conceptual plunging model assumes (a) that the receiving ambient water is well-mixed in the plunging region and (b) that the Fr_d at the inflow is large enough for the momentum of the inflowing river water to cause a plunging that happens in the lake. Ambient water stratification (layered or continuous) and its relative strength could cause changes in the proposed conceptual model, such as modifications in the flow separation and the upwelling of sediment billows, with the formation of horizontal intrusions if the sediment billows cannot reach the surface. The triangle-shaped surface pattern is expected to remain a feature for all $Fr_d > 1$ at the inflow (as numerically simulated by Shi, 2023, for Fr_d values between 2 and 8), with its length becoming shorter for decreasing Fr_d values until the limit of $Fr_d = 1$. At this limit the plunge curve will have reduced to a straight line.
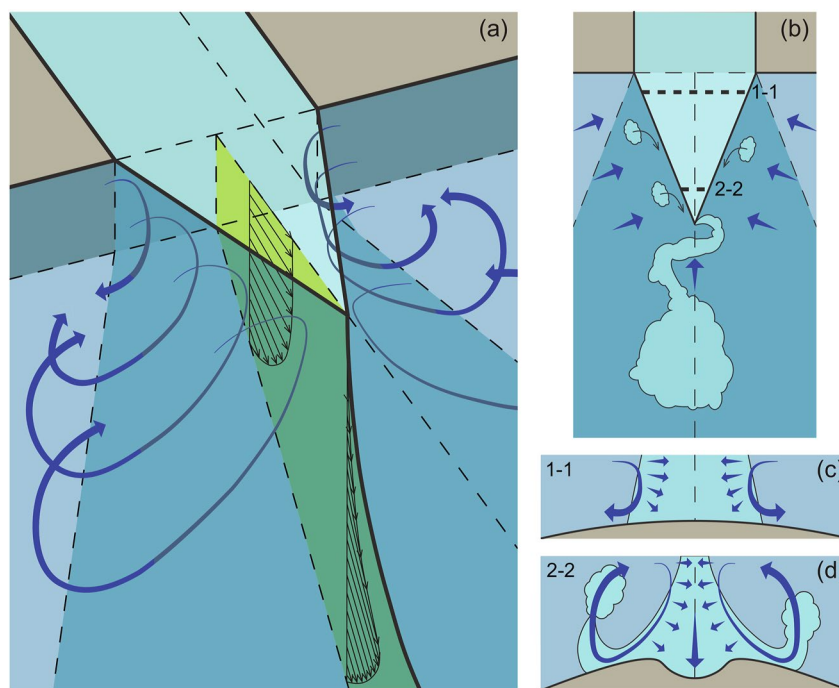
Figure 12. Conceptual model of a laterally unconfined, sediment-laden plunging river inflow. (a) 3-D view. (b) Top-view. (c) Lateral-vertical transect 1-1 close to the river mouth (analogous to transect B-B in Figure 9). (d) Lateral-vertical transect 2-2 further away from the river mouth (analogous to transect D-D in Figure 9). The locations of transects 1-1 and 2-2 are indicated in panel (b). The longitudinal centerline velocity profiles at transect 1-1 and 2-2 are shown in panel (a). The blue curved arrows in panels (a, c, d) indicate the suggested transport pattern of the sediment laden plume water masses outside the plume. The blue straight arrows in panel (b) indicate the suggested return current in the near-surface layer. The blue straight arrows in panels (c, d) indicate the suggested lateral flow convergence over the whole water column. Neither the thickness, nor the length of the blue arrows indicate velocity magnitudes and exist for esthetic purposes only.

Appendix A: Examples of Laterally Unconfined Plunging River Inflows Producing Triangle-Shaped Surface Patterns

A list of 27 examples of riverine inflows whose sediment-rich plumes were found to produce one or multiple triangle-shaped patterns at the surface of the receiving water body was compiled in Table A1.

Table A1
Listing of Examples of Laterally Unconfined River Inflows Whose Plumes Produce Triangle-Shaped Sediment-Rich Patterns at the Surface of the Receiving Water Body

Region	Country	Receiving water body	Inflow	Latitude	Longitude	Google earth imagery date (dd/mm/yyyy)
Africa	Uganda	Lake Victoria	Kagera River	0°56′37.43″S	31°46′55.84″E	11/02/2010
	Burundi	Lake Tanganyika	Rusizi River	3°21′56.29″S	29°16′4.26″E	03/02/2019*
						28/01/2021
Asia	Iraq	Lake Thartar	Thartar Canal	33°50′23.90″N	43°28′37.67″E	26/05/2009
Europe	Austria	Lake Constance	Rhine River	47°31′35.10″N	9°38′40.68″E	02/04/2012
	Germany	Lake Ammer	Ammer River	47°56′43.19″N	11°8′25.09″E	18/05/2020
		Lake Chiem	Großache River	47°51′52.87″N	12°30′23.44″E	21/07/2010
				47°51′35.14″N	12°29′21.40″E	15/04/2015
	Italy	Lake Como	Adda River	46°9′7.12″N	9°22′26.52″E	04/05/2008
		Lake Iseo	Italsider Canal	45°48′24.74″N	10°5′59.53″E	01/01/2022
		Lake Maggiore	Toce River	45°56′10.19″N	8°29′37.90″E	09/07/2022

Table A1
Continued

Region	Country	Receiving water body	Inflow	Latitude	Longitude	Google earth imagery date (dd/mm/yyyy)
	Switzerland	Lake Brienz	Aare River	46°44′33.10″N	8°2′50.80″E	19/07/2010
			Lütschine River	46°41′27.45″N	7°53′53.31″E	04/10/2009
		Lake Geneva	Rhône River	46°23′41.34″N	6°51′31.46″E	04/10/2009
		Lake Lucerne	Reuss River	46°53′56.29″N	8°36′44.61″E	24/08/2017
		Lake Thun	Aare River	46°40′2.07″N	7°49′38.52″E	04/10/2009
				46°39′56.86″N	7°49′39.65″E	04/10/2009
North America	USA	Lake Harrison	Lilloet River	49°44′35.39″N	122°8′47.26″W	02/09/2019
		Lake Lillooet	Lilloet River	50°17′53.41″N	122°35′49.50″W	30/09/2019
		Lake Mead	Colorado River	36°7′49.95″N	114°5′57.32″W	05/06/2010
Oceania	New Zealand	Lake Taupo	Tauranga Taupo River	38°54′25.89″S	175°54′10.70″E	05/06/2019
		Lake Tasman	Tasman River	43°54′15.71″S	170°9′50.06″E	06/01/2022
		Lake Wakatipu	Dart River	44°50′43.72″S	168°21′4.54″E	07/01/2019
South America	Argentina	Lake Los Barreales	Neuquén River	38°28′15.62″S	68°56′0.85″W	03/01/2005
		Lake Viedma	Condor River	49°38′37.78″S	72°35′46.55″W	26/10/2018
	Chile	Lake General Carrera	(unknown)	46°46′46.23″S	72°48′23.80″W	11/04/2016
			Leones River	46°45′46.76″S	72°47′23.12″W	05/12/2018*
		Lake Plomo	Soler River	47°0′25.57″S	72°58′46.50″W	13/01/2019*

Note. The dates marked with an asterisk (*) indicate images in which multiple plumes coalesce to form a single surface pattern with a scalloped edge. Source: Google Earth Pro.

Data Availability Statement

The data discussed in this paper and the MATLAB scripts used for their treatment and analysis can be downloaded from https://www.doi.org/10.48436/2cd8d-bmd42 (Thorez et al., 2023).

References

Akiyama, J., & Stefan, H. G. (1984). Plunging flow into a reservoir: Theory. *Journal of Hydraulic Engineering*, *110*(4), 484–499. https://doi.org/10.1061/(ASCE)0733-9429(1984)110:4(484)

Akiyama, J., & Stefan, H. G. (1987). Onset of underflow in slightly diverging channels. *Journal of Hydraulic Engineering*, *113*(7), 825–843. https://doi.org/10.1061/(ASCE)0733-9429(1987)113:7(825)

Alavian, V. (1986). Behavior of density currents on an incline. *Journal of Hydraulic Engineering*, *112*(1), 27–42. https://doi.org/10.1061/(ASCE)0733-9429(1986)112:1(27)

Allan, R. J., Mudroch, A., & Sudar, A. (1983). An introduction to the Niagara River/Lake Ontario pollution problem. *Journal of Great Lakes Research*, *9*(2), 111–117. https://doi.org/10.1016/S0380-1330(83)71881-2

Arita, M., & Nakai, M. (2008). Plunging conditions of two-dimensional negative buoyant surface jets released on a sloping bottom. *Journal of Hydraulic Research*, *46*(3), 301–306. https://doi.org/10.3826/jhr.2008.2714

Best, J. L., Kostaschuk, R. A., Peakall, J., Villard, P. V., & Franklin, M. (2005). Whole flow field dynamics and velocity pulsing within natural sediment-laden underflows. *Geology*, *33*(10), 765–768. https://doi.org/10.1130/G21516.1

Bresse, J. A. C. (1860). *Cours de mecanique appliquee: 2: Hydraulique*. Mallet-Bachelier.

Broekema, Y. B., Labeur, R. J., & Uijttewaal, W. S. J. (2020). Suppression of vertical flow separation over steep slopes in open channels by horizontal flow contraction. *Journal of Fluid Mechanics*, *885*, A8. https://doi.org/10.1017/jfm.2019.972

Brown, P. P., & Lawler, D. F. (2003). Sphere drag and settling velocity revisited. *Journal of Environmental Engineering*, *129*(3), 222–231. https://doi.org/10.1061/(ASCE)0733-9372(2003)129:3(222)

Burrus, D., Thomas, R. L., Dominik, J., & Vernet, J.-P. (1989). Recovery and concentration of suspended solids in the Upper Rhone River by continuous flow centrifugation. *Hydrological Processes*, *3*(1), 65–74. https://doi.org/10.1002/hyp.3360030107

Chen, C.-T. A., & Millero, F. J. (1986). Precise thermodynamic properties for natural waters covering only the limnological range. *Limnology & Oceanography*, *31*(3), 657–662. https://doi.org/10.4319/lo.1986.31.3.0657

Corella, J. P., Arantegui, A., Loizeau, J. L., DelSontro, T., le Dantec, N., Stark, N., et al. (2014). Sediment dynamics in the subaquatic channel of the Rhone delta (Lake Geneva, France/Switzerland). *Aquatic Sciences*, *76*(S1), 73–87. https://doi.org/10.1007/s00027-013-0309-4

Cortés, A., Fleenor, W. E., Wells, M. G., de Vicente, I., & Rueda, F. J. (2014). Pathways of river water to the surface layers of stratified reservoirs. *Limnology & Oceanography*, *59*(1), 233–250. https://doi.org/10.4319/lo.2014.59.1.0233

Duguay, J., Biron, P. M., & Lacey, J. (2022). Aerial observations and numerical simulations confirm density-driven streamwise vortices at a river confluence. *Water Resources Research*, *58*(7), e2021WR031527. https://doi.org/10.1029/2021WR031527

Duringer, P., Paicheler, J. C., & Schneider, J. L. (1991). Un courant d'eau continu peut-il générer des turbidites? Résultats d'expérimentations analogiques. *Marine Geology*, *99*(1–2), 231–246. https://doi.org/10.1016/0025-3227(91)90093-J

Elder, R. A., & Wunderlich, W. O. (1972). Inflow density currents in TVA reservoirs. In *ASCE proceedings, international symposium of stratified flow* (pp. 221–236). Ellison.

Fink, G., Wessels, M., & Wüest, A. (2016). Flood frequency matters: Why climate change degrades deep-water quality of peri-alpine lakes. *Journal of Hydrology*, *540*, 457–468. https://doi.org/10.1016/j.jhydrol.2016.06.023

Fischer, H. B., List, E. J., Koh, R. C. Y., Imberger, J., & Brooks, N. H. (1979). *Mixing in inland and coastal waters*. Academic Press. https://doi.org/10.1016/C2009-0-22051-4

Fischer, H. B., & Smith, R. D. (1983). Observations of transport to surface waters from a plunging inflow to Lake Mead. *Limnology & Oceanography*, *28*(2), 258–272. https://doi.org/10.4319/lo.1983.28.2.0258

Fleenor, W. E. (2001). *Effects and control of plunging inflows on reservoir hydrodynamics and downstream releases* (Doctoral dissertation). University of California. Retrieved from https://search.library.ucdavis.edu/permalink/01UCD_INST/9fle3i/alma990021089970403126

Forel, F. A. (1885). Les ravins sous-lacustres des fleuves glaciaires. *Comptes Rendus de l'Académie des Sciences*, *101*, 725–728. https://doi.org/10.5169/seals-12049

Forel, F. A. (1892). *Le Léman*. https://doi.org/10.3931/e-rara-49502

Fromant, G. (2019). HYDRAC [Software]. Bitbucket. https://bitbucket.org/fromantgu/hydrac/src/master/

Fromant, G., Hurther, D., le Dantec, N., Lebourges-Dhaussy, A., Jourdin, F., Vergnes, A., et al. (2020). Hydrac, an inversion software for SPM quantification. In *River Flow 2020* (pp. 340–348). CRC Press. https://doi.org/10.1201/b22619-49

Girardclos, S., Hilbe, M., Corella, J. P., Loizeau, J. L., Kremer, K., Delsontro, T., et al. (2012). Searching the Rhone delta channel in Lake Geneva since François Alphonse FOREL. *Archives Des Sciences*, *65*(1–2), 103–118. https://doi.org/10.7892/boris.45630

Graf, W. H. (1998). *Fluvial hydraulics: Flow and transport processes in channels of simple geometry* (1st ed.). John Wiley & Sons Ltd.

Hauenstein, W. (1983). *Zuflussbedingte Dichteströmungen in seen* (Doctoral dissertation). ETH Zürich. Retrieved from https://eth.swisscovery.slsp.ch/permalink/41SLSP_ETH/lshl64/alma990003139310205503

Hauenstein, W., & Dracos, T. (1984). Investigation of plunging density currents generated by inflows in lakes. *Journal of Hydraulic Research*, *22*(3), 157–179. https://doi.org/10.1080/00221688409499404

Hebbert, B., Patterson, J., Loh, I., & Imberger, J. (1979). Collie River underflow into the Wellington reservoir. *Journal of the Hydraulics Division*, *105*(5), 533–545. https://doi.org/10.1061/JYCEAJ.0005206

Hogg, C. A. R. (2014). *The flow of rivers into lakes: Experiments and models* (Doctoral dissertation). University of Cambridge. https://doi.org/10.17863/CAM.32

Hogg, C. A. R., Marti, C. L., Huppert, H. E., & Imberger, J. (2013). Mixing of an interflow into the ambient water of Lake Iseo. *Limnology & Oceanography*, *58*(2), 579–592. https://doi.org/10.4319/lo.2013.58.2.0579

Johnson, T. R., Ellis, C. R., Farrell, G. J., & Stefan, H. G. (1987). Negatively buoyant flow in a diverging channel. II: 3-d flow field descriptions. *Journal of Hydraulic Engineering*, *113*(6), 731–742. https://doi.org/10.1061/(ASCE)0733-9429(1987)113:6(731)

Johnson, T. R., Ellis, C. R., & Stefan, H. G. (1989). Negatively buoyant flow in diverging channel, IV: Entrainment and dilution. *Journal of Hydraulic Engineering*, *115*(4), 437–456. https://doi.org/10.1061/(ASCE)0733-9429(1989)115:4(437)

Johnson, T. R., Farrell, G. J., Ellis, C. R., & Stefan, H. G. (1987). Negatively buoyant flow in a diverging channel. I: Flow regimes. *Journal of Hydraulic Engineering*, *113*(6), 716–730. https://doi.org/10.1061/(ASCE)0733-9429(1987)113:6(716)

Katz, T., Ginat, H., Eyal, G., Steiner, Z., Braun, Y., Shalev, S., & Goodman-Tchernov, B. N. (2015). Desert flash floods form hyperpycnal flows in the coral-rich Gulf of Aqaba, Red Sea. *Earth and Planetary Science Letters*, *417*, 87–98. https://doi.org/10.1016/j.epsl.2015.02.025

Kostaschuk, R., Nasr-Azadani, M. M., Meiburg, E., Wei, T., Chen, Z., Negretti, M. E., et al. (2018). On the causes of pulsing in continuous turbidity currents. *Journal of Geophysical Research: Earth Surface*, *123*(11), 2827–2843. https://doi.org/10.1029/2018JF004719

Lamb, M. P., McElroy, B., Kopriva, B., Shaw, J., & Mohrig, D. (2010). Linking river-flood dynamics to hyperpycnal-plume deposits: Experiments, theory, and geological implications. *Bulletin of the Geological Society of America*, *122*(9–10), 1389–1400. https://doi.org/10.1130/B30125.1

Lambert, A., & Giovanoli, F. (1988). Records of riverborne turbidity currents and indications of slope failures in the Rhone delta of Lake Geneva. *Limnology & Oceanography*, *33*(3), 458–468. https://doi.org/10.4319/lo.1988.33.3.0458

Lambert, A., Kelts, K., & Zimmermann, U. (1984). Trübeströme in Seen: Sauerstoffeintrag durch grundnah eingeschichtetes Flusswasser. *Schweizerische Zeitschrift für Hydrologie*, *46*(1), 41–50. https://doi.org/10.1007/BF02538097

Lee, H.-Y., & Yu, W.-S. (1997). Experimental study of reservoir turbidity current. *Journal of Hydraulic Engineering*, *123*(6), 520–528. https://doi.org/10.1061/(ASCE)0733-9429(1997)123:6(520)

Lemmin, U., & D'Adamo, N. (1996). Summertime winds and direct cyclonic circulation: Observations from Lake Geneva. *Annales Geophysicae*, *14*(11), 1207–1220. https://doi.org/10.1007/s00585-996-1207-z

Loizeau, J. L., & Dominik, J. (2000). Evolution of the Upper Rhone River discharge and suspended sediment load during the last 80 years and some implications for Lake Geneva. *Aquatic Sciences*, *62*(1), 54–67. https://doi.org/10.1007/s000270050075

Mulder, T., Syvitski, J. P. M., Migeon, S., Faugères, J. C., & Savoye, B. (2003). Marine hyperpycnal flows: Initiation, behaviorand related deposits. A review. *Marine and Petroleum Geology*, *20*(6–8), 861–882. https://doi.org/10.1016/j.marpetgeo.2003.01.003

Parker, G., Fukushima, Y., & Pantin, H. M. (1986). Self-accelerating turbidity currents. *Journal of Fluid Mechanics*, *171*(1), 145. https://doi.org/10.1017/S0022112086001404

Piton, V., Soulignac, F., Lemmin, U., Graf, B., Wynn, H. K., Blanckaert, K., & Barry, D. A. (2022). Tracing unconfined nearfield spreading of a river plume interflow in a large lake (Lake Geneva): Hydrodynamics, suspended particulate matter, and associated fluxes. *Frontiers in Water*, *4*, 943242. https://doi.org/10.3389/frwa.2022.943242

Rimet, F., Anneville, O., Barbet, D., Chardon, C., Crépin, L., Domaizon, I., et al. (2020). The Observatory on LAkes (OLA) database: Sixty years of environmental data accessible to the public. *Journal of Limnology*, *79*(2), 164–178. https://doi.org/10.4081/jlimnol.2020.1944

Rueda, F. J., Fleenor, W. E., & de Vicente, I. (2007). Pathways of river nutrients towards the euphotic zone in a deep-reservoir of small size: Uncertainty analysis. *Ecological Modelling*, *202*(3–4), 345–361. https://doi.org/10.1016/j.ecolmodel.2006.11.006

Schleiss, A. J., Franca, M. J., Juez, C., & de Cesare, G. (2016). Reservoir sedimentation. *Journal of Hydraulic Research*, *54*(6), 595–614. https://doi.org/10.1080/00221686.2016.1225320

Schuch, F. N., Meiburg, E., & Silvestrini, J. H. (2021). Plunging criterion for particle-laden flows over sloping bottoms: Three-dimensional turbulence-resolving simulations. *Computers & Geosciences*, *156*, 104880. https://doi.org/10.1016/j.cageo.2021.104880

Schuch, F. N., Pinto, L. C., Silvestrini, J. H., & Laizet, S. (2018). Three-dimensional turbulence-resolving simulations of the plunge phenomenon in a tilted channel. *Journal of Geophysical Research: Oceans*, *123*(7), 4820–4832. https://doi.org/10.1029/2018JC014027

Sequeiros, O. E., Spinewine, B., Beaubouef, R. T., Sun, T., García, M. H., & Parker, G. (2010). Characteristics of velocity and excess density profiles of saline underflows and turbidity currents flowing over a mobile bed. *Journal of Hydraulic Engineering*, *136*(7), 412–433. https://doi.org/10.1061/(asce)hy.1943-7900.0000200

Shi, H. (2023). *Laterally unconfined neutral or negative buoyancy inflow into a quiescent ambient over sloping bottom* (Doctoral dissertation). EPFL. https://doi.org/10.5075/epfl-thesis-10453

Shi, H., Negretti, M. E., Chauchat, J., Blanckaert, K., Lemmin, U., & Barry, D. A. (2022). Unconfined plunging of a hyperpycnal river plume over a sloping bed and its lateral spreading: Laboratory experiments and numerical modeling. *Water Resources Research*, *58*(8), e2022WR032633. https://doi.org/10.1029/2022wr032633

Singh, B., & Shah, C. R. (1971). Plunging phenomenon of density currents in reservoirs. *La Houille Blanche*, *57*(1), 59–64. https://doi.org/10.1051/lhb/1971005

Soulignac, F., Lemmin, U., Ziabari, S. M. H., Wynn, H. K., Graf, B., & Barry, D. A. (2021). Rapid changes in river plume dynamics caused by advected wind-driven coastal upwelling as observed in Lake Geneva. *Limnology & Oceanography*, *66*(8), 3116–3133. https://doi.org/10.1002/lno.11864

Spigel, R. H., Howard-Williams, C., Gibbs, M., Stephens, S., & Waugh, B. (2005). Field calibration of a formula for entrance mixing of river inflows to lakes: Lake Taupo, North Island, New Zealand. *New Zealand Journal of Marine & Freshwater Research*, *39*(4), 785–802. https://doi.org/10.1080/00288330.2005.9517353

Stefan, H. G., & Johnson, T. R. (1989). Negatively buoyant flow in diverging channel. III: Onset of underflow. *Journal of Hydraulic Engineering*, *115*(4), 423–436. https://doi.org/10.1061/(ASCE)0733-9429(1989)115:4(423)

TeChow, V. (1959). *Open-channel hydraulics*. McGraw-Hill.

Thorez, S., Lemmin, U., Barry, D. A., & Blanckaert, K. (2023). Hydro-sedimentary processes of a plunging hyperpycnal river plume revealed by synchronized remote imagery and gridded current measurements - Supporting data and scripts (1.1.0) [Dataset]. TU Wien. https://www.doi.org/10.48436/2cd8d-bmd42

Tiercelin, J. J., Soreghan, M., Cohen, A. S., Lezzar, K.-E., & Bouroullec, J.-L. (1992). Sedimentation in large rift lakes: Example from the middle pleistocene–Modern deposits of the Tanganyika trough, East African Rift system. *Bulletin - Centre de Recherche Exploration-Production Elf-Aquitaine*, *16*(1), 83–111.

Tiercelin, J. J., Vincens, A., Barton, C. E., Carbonel, P., Casanova, J., Delibrias, G., et al. (1987). Le demi-graben de Baringo-Bogoria, Rift Gregory, Kenya 30 000 ans d'histoire hydrologique et sedimentaire. *Bulletin - Centres de Recherche Exploration-Production Elf- Aquitaine*, *11*(2), 249–540.

Tseng, C. Y., & Chou, Y. J. (2018). Nonhydrostatic simulation of hyperpycnal river plumes on sloping continental shelves: Flow structures and nonhydrostatic effect. *Ocean Modelling*, *124*(February), 33–47. https://doi.org/10.1016/j.ocemod.2018.02.003

Vermeulen, B. (2015). adcptools [Software]. SourceForge. https://sourceforge.net/projects/adcptools/

Vermeulen, B., Sassi, M. G., & Hoitink, A. J. F. (2014). Improved flow velocity estimates from moving-boat ADCP measurements. *Water Resources Research*, *50*(5), 4186–4196. https://doi.org/10.1002/2013WR015152

Vidal, J., Marcé, R., Serra, T., Colomer, J., Rueda, F., & Casamitjana, X. (2012). Localized algal blooms induced by river inflows in a canyon type reservoir. *Aquatic Sciences*, *74*(2), 315–327. https://doi.org/10.1007/s00027-011-0223-6

Vincent, W. F., Gibbs, M. M., & Spigel, R. H. (1991). Eutrophication processes regulated by a plunging river inflow. *Hydrobiologia*, *226*(1), 51–63. https://doi.org/10.1007/BF00007779

Wüest, A., Imboden, D. M., & Schurter, M. (1988). Origin and size of hypolimnic mixing in Urnersee, the southern basin of Vierwaldstättersee (Lake Lucerne). *Swiss Journal of Hydrology*, *50*(1), 40–70. https://doi.org/10.1007/BF02538371

Wurtsbaugh, W. A., Paerl, H. W., & Dodds, W. K. (2019). Nutrients, eutrophication and harmful algal blooms along the freshwater to marine continuum. *WIREs Water*, *6*(5), e1373. https://doi.org/10.1002/wat2.1373